Photoinduced transitions in magnetoresistive manganites: A comprehensive view

V. Esposito,[1,*] L. Rettig,[1,2] E. Abreu,[3] E. M. Bothschafter,[1] G. Ingold,[1,4] M. Kawasaki,[5,6] M. Kubli,[3] G. Lantz,[3]
M. Nakamura,[5,7] J. Rittman,[1,4] M. Savoini,[3] Y. Tokura,[5,6] U. Staub,[1] S. L. Johnson,[3] and P. Beaud[1,4,†]

[1]*Swiss Light Source, Paul Scherrer Institut, 5232 Villigen PSI, Switzerland*
[2]*Fritz Haber Institute, 14195 Berlin, Germany*
[3]*Institute for Quantum Electronics, ETH Zürich, 8093 Zürich, Switzerland*
[4]*SwissFEL, Paul Scherrer Institut, 5232 Villigen PSI, Switzerland*
[5]*RIKEN Center for Emergent Matter Science, Wako 351-0198, Japan*
[6]*Department of Applied Physics and Quantum Phase Electronics Center (QPEC), University of Tokyo, Tokyo 113-8656, Japan*
[7]*PRESTO, Japan Science and Technology Agency (JST), Kawaguchi, 332-0012, Japan*

We use femtosecond x-ray diffraction to study the structural response of charge and orbitally ordered $Pr_{1-x}Ca_xMnO_3$ thin films across a phase transition induced by 800 nm laser pulses. By investigating the dynamics of both superlattice reflections and regular Bragg peaks, we disentangle the different structural contributions and analyze their relevant timescales. The dynamics of the structural and charge order response are qualitatively different when excited above and below a critical fluence f_c. For excitations below f_c the charge order and the superlattice is only partially suppressed and the ground state recovers within a few tens of nanosecond via diffusive cooling. When exciting above the critical fluence the superlattice vanishes within approximately half a picosecond followed by a change of the unit cell parameters on a 10 picoseconds timescale. At this point all memory from the symmetry breaking is lost and the recovery time increases by many order of magnitudes due to the first order character of the structural phase transition.

I. INTRODUCTION

Nonthermal control of materials properties is key in developing technologically relevant applications. Notable examples are field-effect transistors and magnetic storage, where the properties of the device are controlled by an applied voltage or a magnetic field, respectively. Ultrashort light pulses have also been used to create nonthermal metastable states, and this approach has been successfully applied to induce insulator-to-metal transitions [1–4] and to control superconductivity [5–7], ferroelectric polarization [8,9] or magnetic properties [10–13]. In these cases, however, the relaxation towards the ground state of the material does often not happen in a controlled manner and instead depends on intrinsic material properties. Understanding the underlying physics and timescales of both the excitation process and the recovery mechanisms is thus of crucial importance to push toward potential technological applications.

The colossal magnetoresistance effect found in doped manganites is a well-known example of such a nonthermal effect. Magnetoresistive manganites exhibit a large variety of ordering phenomena as a function of doping and temperature due to the complex interplay between the charge, orbital, spin, and structural degrees of freedom. At low temperature, two possible ground states are in competition: a ferromagnetic metallic phase and an antiferromagnetic, charge- and orbital-ordered insulating phase. The observed colossal magnetoresis-

tance and the insulator-to-metal transition that occur in these materials are thought to be strongly related to this competition [14]. Photoinduced transitions have been reported following the ultrafast excitation of the electronic system, with similar responses found when either the interatomic O $2p$-Mn $3d$ e_g charge-transfer resonance [15] or the intra-atomic Mn $3d$ transitions are excited [16]. This insulator-to-metal transition [1,17] is accompanied by a relaxation of the structural distortion [16,18] induced by the prompt suppression of the charge and orbital order [19]. The spin ordering is also significantly altered after photoexcitation. The antiferromagnetic order is melted [20–22] and ferromagnetic correlations emerge [23,24]. Other excitation mechanisms such as resonant excitation of the lattice [21,25,26], pulsed magnetic fields [27], intense x-ray radiation [28,29], or static illumination [30] also dramatically alter the electronic, structural, and magnetic properties of these manganites.

In this paper we focus on the picosecond timescale structural dynamics that follow the initial nonthermal melting of the superlattice in the three-dimensional charge and orbitally ordered manganite $Pr_{1-x}Ca_xMnO_3$ ($x = 0.5$, 0.4, 0.35). The charge and orbital ordered (COO) state that emerges below T_{COO} consists of a checkerboard pattern of Mn^{3+} and Mn^{4+} in the ab plane and the alignment of the Mn^{3+} $3z^2 - r^2$ orbitals in a zigzag pattern along the *Pbnm b* axis. This first order transition induces a Jahn-Teller (JT) distortion on the Mn^{3+} sites, leading to a lowering of the crystal symmetry from orthorhombic *Pbnm* to monoclinic $P2_1/m$ [31]. The COO state and a sketch of the Mn electronic configurations are shown in Figs. 1(a) and 1(b). Because of the doubling of the unit cell along the crystallographic *b* axis, this transition is directly

*Corresponding author: vincent.esposito@psi.ch
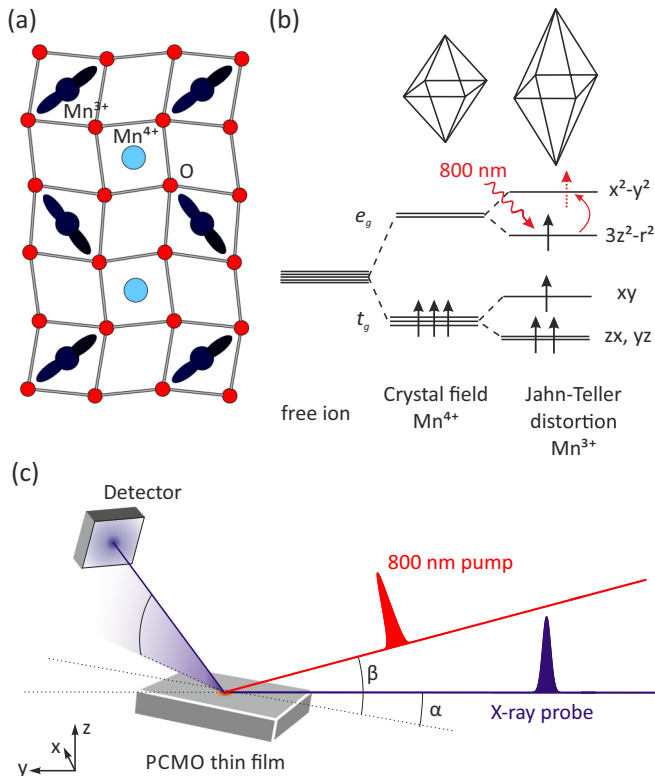†Corresponding author: paul.beaud@psi.ch

FIG. 1. (a) Charge and orbital order in PCMO in the *ab* plane. The apical oxygens and the rare-earth ions are omitted here for the sake of clarity. (b) Electronic structure of the *d* orbitals of manganese as a function of the orbital occupancy and the corresponding distortion of the surrounding oxygen octahedra. The electronic transition induced by the 1.55 eV pump laser is indicated by the red arrow. (c) Sketch of the grazing incidence experimental setup for time-resolved x-ray diffraction. The incident angles α and β are 0.5 and 10 degrees, respectively.

source produces pulses of about 140 femtoseconds duration from electrons that are modulated by a short laser pulse in the storage ring. A sketch of the experimental setup is shown in Fig. 1(c). Using a double Mo/B_4C multilayer monochromator the x-ray energy was set to 7 keV, a good compromise between the optimal source flux and minimum air-transmission losses. The penetration depth of the pump and the probe were matched by a small 0.5 degree incident angle of the x-ray beam, and the footprint on the sample was minimized by small vertical focus of the beam of 10 μm [37]. The beam remained unfocussed horizontally with a width of about 300 μm. The sample was excited with weakly-focused (520×620 μm^2) *p*-polarized 100-fs pulses at 800-nm wavelength entering the sample at 10 degrees grazing incidence. The angle mismatch between the pump and the probe increases the time resolution to approximately 150 fs. The repetition rates of the optical pump and the x-ray probe were 1 and 2 kHz, respectively. In this way the probed signal alternates between pumped and unpumped states of the sample, allowing us to compensate for slow drifts in the x-ray source, pump laser, detector, and electronics [38].

The diffracted intensity of superlattice peaks was measured with an avalanche photodiode (APD), providing enhanced sensitivity for weak signals. In addition to the APD, the Pilatus pixel detector [39] was used in gated mode to investigate the more intense regular Bragg reflections. Both detectors provide a photon-counting operation mode that is well suited for these low flux diffraction experiments. In addition the pixel detector allows us to map the peak displacements in reciprocal space, disentangling in-plane and out-of-plane motions. The x-ray energy is above the Mn *K* edge and therefore x-ray fluorescence contributes significantly to a homogeneous background. For the data taken with the two-dimensional detector, the background is given by a featureless region of interest in the images, while in the case of the APD point detector, it is estimated from the constant baseline of the rocking curve scans.

III. RESULTS AND DISCUSSION

Our results are discussed in four subsections, which correspond to the dynamics at different timescales. First the subpicosecond structural dynamics is examined. On this timescale, the atomic motions are limited to isochoric dynamics, involving small atomic motion carried by coherent optical phonons that do not alter the dimensions of the underlying unit cell. In a second section, we investigate the picosecond dynamics of the lattice and reveal a second step of the structural transition. This slower component of the phase transition includes a change of the crystallographic unit cell from the low temperature monoclinic structure to the high temperature orthorhombic cell. Finally, we discuss the recovery to the COO ground state, before pointing at a possible unique description linked to ferromagnetism in a last section.

A. The ultrafast isochoric transition

An overview of the fluence dependence of the dynamics of the $(\bar{2}\frac{\bar{3}}{2}0)$ superlattice reflection of the PCMO films is given in Fig. 2 for two doping concentrations $x = 0.5$ and 0.4. This type of reflections emerge as a direct consequence of
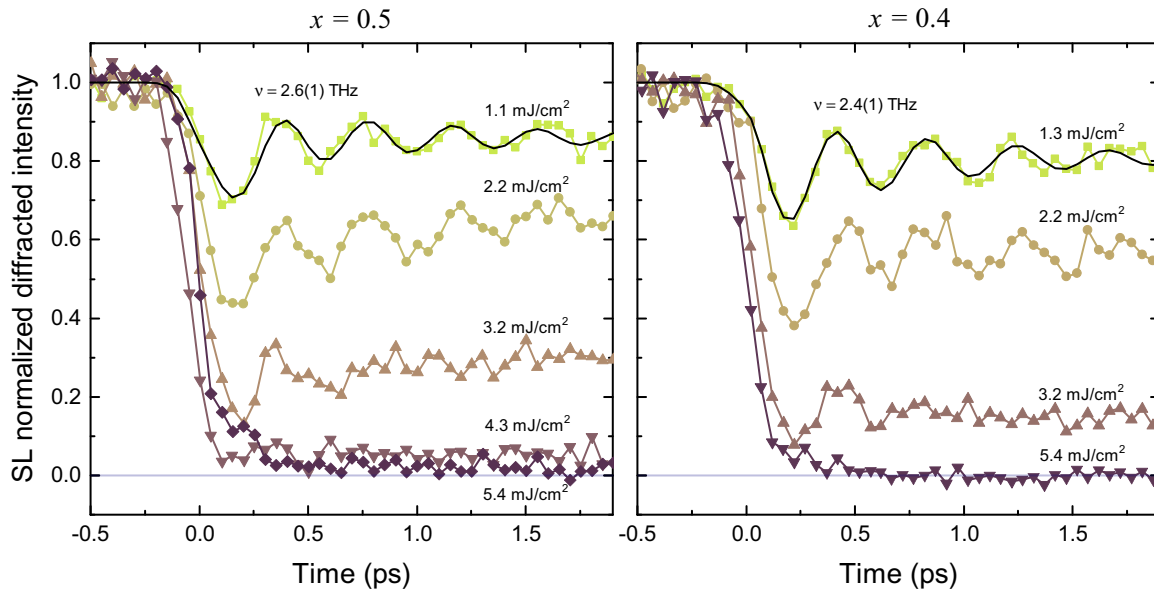
observable in x-ray diffraction experiments by the appearance of superlattice (SL) reflections of the type $(h\frac{k}{2}l)$ [32,33]. A second order transition to a CE-type antiferromagnetic order occurs at the Néel temperature $T_N < T_{COO}$ [14,34].

Our study discusses not only the entire phase transition to the higher symmetry state but also the recovery back to the initial lower symmetry state. Together with the result of previous studies this investigation proposes a unified picture for this photoinduced nonequilibrium phase transition.

II. EXPERIMENTAL DETAILS

The 40-nm-thick PCMO thin films were grown by pulsed laser deposition on (011)-oriented $(LaAlO_3)_{0.3}(SrAl_{0.5}Ta_{0.5}O_3)_{0.7}$ substrates [35]. Two samples with different doping concentration ($x = 0.5$ and 0.4) were investigated in this work. The COO transition temperatures were characterized by transport measurement yielding $T_{CO} = 221$ and 206 K, respectively. In the diffraction experiments reported here the sample was cooled down to 100 K with a nitrogen cryoblower.

The time-resolved x-ray experiments were carried out at the FEMTO slicing source at the Swiss Light Source [36]. This

FIG. 2. Time dependence of the diffracted intensity of the $(\bar{2}\frac{\bar{3}}{2}0)$ superlattice reflection at 100 K for different pump fluences and doping concentrations x. The black lines are fits used to extract the frequency ν of the observed coherent oscillation.

the doubling of the unit cell below the ordering temperature. Their structure factors thus provide direct information on the magnitude of the low temperature structural distortion. All three doping concentrations display qualitatively similar time dependences following photoexcitation: a fast drop in intensity for all fluences and a clear prominent coherent 2.5 THz oscillation at low and intermediate fluences. The data for the two doping concentrations are very similar and the peak intensity disappears in both cases for fluences above about 5 mJ/cm^2.

For the $x = 0.5$ sample, the dynamics and critical behavior are consistent with a previous study of the charge order and lattice dynamics [19]. The superlattice peak disappears at times $t > 0.5$ ps for fluences above $f'_c \approx 5$ mJ/cm^2. Assuming linear absorption, the excitation profile is given by

$$f(z) = f_0 e^{-z/z_0}, \qquad (1)$$

where $z_0 = 48$ nm is the effective penetration depth, accounting for the shallow incident angle. The effective fluence seen by the deepest layer is thus $f_c \approx 2.4$ mJ/cm^2, corresponding to the critical fluence at which the charge and orbital order melts at the surface [19]. For intermediate fluences between f_c and f'_c, there is a coexistence of melted and nonmelted layers (inset Fig. 3).

The critical fluences can be also fitted in the fluence-dependent drop of the superlattice intensity at 20 ps (Fig. 3). In equilibrium the structure factor of the superlattice reflection is an order parameter of the structurally distorted phase. Out of equilibrium this is however not always the case, as the transient structure does not necessarily correspond to a minimum of the potential energy surface. In our experiment, the oscillatory dynamics are gone after a few picoseconds, suggesting that the dynamical component of the response has damped out and the structure is effectively tracking the position of a minimum in the potential energy surface. The structure factor F of the reflection is thus modeled by a Landau-like order parameter,

constructed by splitting the film into N layers [19]:

$$F = \frac{1}{N} \sum_{i}^{N} \left(1 - \frac{f(z_i)}{f_c} \right)^{\gamma}, \qquad (2)$$

where the fluence seen by a layer at depth z_i in the sample is given by Eq. (1). The critical fluence f_c and the critical exponent γ are fitted to the data in Fig. 3. A small scaling factor is used to account for the fact that the reflection does not vanish at the highest fluences. The extracted critical fluences are
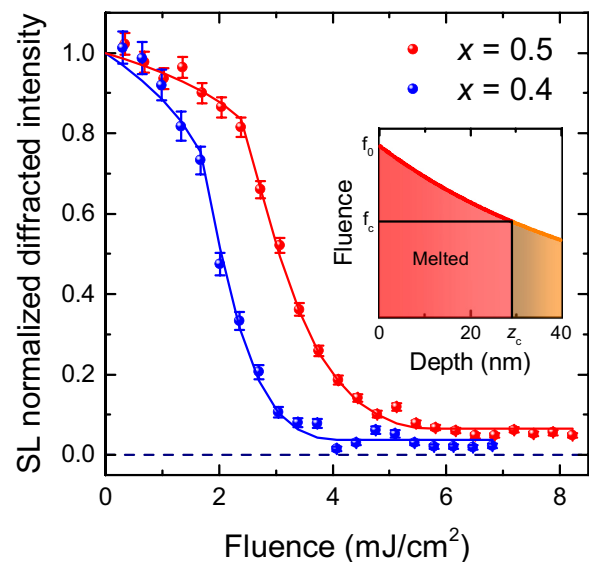

FIG. 3. Fluence scans of the SL peak 20 ps after excitation for the doping concentration $x = 0.5$ (red) and $x = 0.4$ (blue) at 100 K. The lines are fits with a Landau-like order parameter function (cf main text). The inset shows an excitation profile for a surface fluence f_0 between f_c and f'_c, for which the bottom layers of the film experience a fluence below f_c.
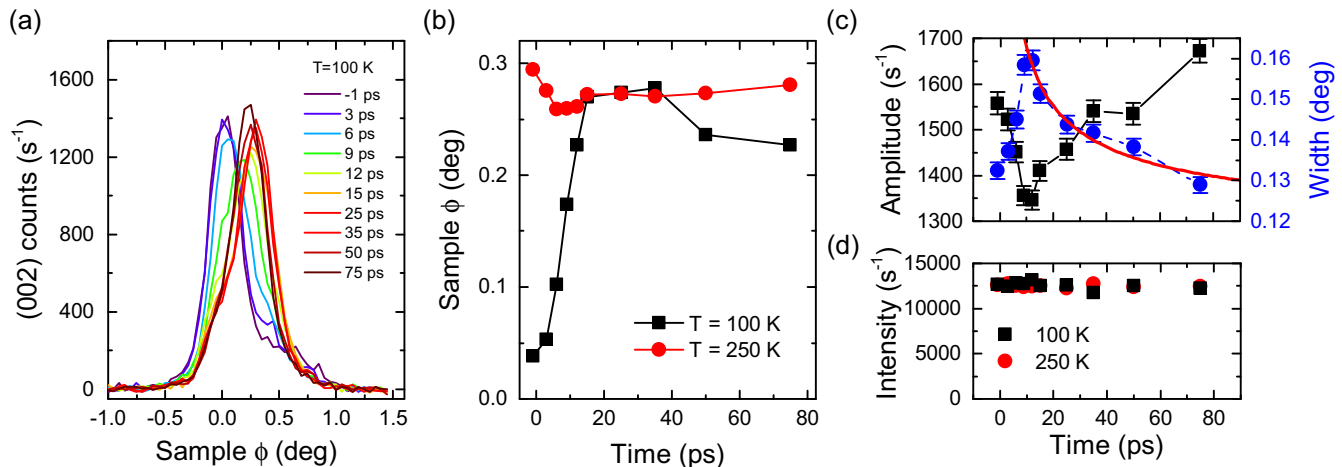
FIG. 4. (a) Time dependence of the (002) Bragg reflection at a fluence of 8.2 mJ/cm^2 ($T = 100$ K). The ϕ axis indicates the sample rotation around its surface normal and the reference ($\phi = 0$) is set to the low temperature peak position. (b) Fitted (002) position as a function of time at 100 K (black squares) and 250 K (red dots). The error bars (not shown) are about the size of the symbols. (c) Amplitude and width of the (002) peak at $T = 100$ K. The red line shows the expected behavior of the peak width for times later than 10 ps and is discussed in the main text. (d) Integrated intensity as a function of time above and below the critical temperature.

$f_c = 2.4(2)$ mJ/cm^2 for the $x = 0.5$ sample and $f_c = 1.7(1)$ mJ/cm^2 for the $x = 0.4$ sample. The fitted critical exponents are $\gamma = 0.17(4)$ and $\gamma = 0.27(6)$, respectively, consistent with similar measurements [19].

The additional holes added when moving away from the optimum half-doped system are often described as defects within the COO pattern [14]. This explains well the lower critical temperature observed for smaller x values, and similarly a lower critical fluence is expected for the photoinduced transition. A lower critical fluence is indeed found for the $x = 0.4$ sample but the overall dynamic response is qualitatively very similar for the different doping concentrations, and we will therefore focus on the following on the half-doped $x = 0.5$ film only.

The subpicosecond dynamics resulting from melting the superlattice in the ground state of mixed valence manganites with an ultrashort 800 nm laser pulse have been extensively discussed in previous works [16,18,19,40]. Our current results are consistent with these studies and here we simply summarize the main conclusions. The ultrashort 1.5 eV excitation effectively removes an electron from the elongated $3z^2 - r^2$ orbital of the Mn^{3+} e_g band and transfers it into the more symmetric $x^2 - y^2$ orbital [Fig. 1(b)]. This initial step instantaneously decreases the orbital order and is followed by a rapid delocalization of the excited e_g electrons, thereby suppressing the charge order [19]. These rapid changes of the electronic properties launch an ultrafast structural phase transition. The fast suppression of COO releases the Jahn-Teller distortions and the superlattice collapses. The sudden collapse drives coherent vibrational motion along several optical A_g phonon mode coordinates [41], ranging in frequency from the Jahn-Teller mode at 14.5 THz to a slow vibrational mode at 2.5 THz that quickly dominates the dynamical response [18,42]. This last frequency is believed to correspond to a 2.7 THz mode observed in equilibrium and attributed to the motion of the rare earth Pr/Ca ions [43]. It was shown, however, that the atomic motion corresponding to the observed 2.5 THz oscillation cannot be exclusively attributed to motion of these ions [40]. The

observed oscillation is rather the result of the renormalization of the excited modes, due to nonlinear phonon coupling [19]. For low excitation, the electronic order and structural distortions are only partially relaxed. But at sufficiently high fluences, the COO is completely destroyed and the potential energy surface shifts towards a high symmetry point, as shown by the complete disappearance of superlattice reflections within 0.5 ps (Fig. 2) [18,19].

B. Monoclinic to orthorhombic transition

In the adiabatic limit, heating the system above T$_{COO}$ includes a change from a monoclinic to orthorhombic lattice in addition to the removal of the superlattice. Such changes, however, involve a change in long range order mediated by long-wavelength acoustic modes and so are expected to develop over a time scale given by the time needed for a sound wave to propagate from the surface and/or domain boundaries across the probed region of the sample, roughly 10 ps [44]. We thus expect that on longer time scales the unit cells should deform to an orthorhombic shape. Superlattice reflections are not adequate to study the changes of the unit cell across a phase transition, since they vanish once the change of superlattice symmetry has occurred. Therefore we chose to measure the (002) Bragg reflection, whose structure factor is only weakly altered by the formation of the superstructure and can be monitored throughout the transition.

The time dependence of the (002) reflection at 100 K, i.e., below T$_{COO}$, is summarized in Fig. 4. In panel (a), the intensity of the reflection is plotted as a function of the sample rotation ϕ for various time delays at an excitation fluence $f = 8.2$ mJ/cm^2, fully sufficient to melt COO and the superlattice in the entire probed volume. An equivalent dataset (not shown) was taken above T$_{COO}$ to compare the induced dynamics in the absence of the structural phase transition. The shoulder around $\phi = 0.5$ degree rotation in Fig. 4(a) matches the high temperature peak position and is attributed to a few strained layers and/or defects, probably near the film/substrate

interface, that do not undergo the transition when cooling the sample. Its large width indicates indeed a small correlation length, as expected from diffraction by a very thin layer.

The peaks were fitted with a symmetric Lorentzian, and the extracted parameters are summarized in panels (b) and (d) of Fig. 4. The Bragg peak position versus time is shown in Fig. 4(b) for temperature above and below T_{COO}. In the high temperature phase, the peak position is almost constant as a function of time with small variations due to lattice heating dynamics and a strain wave traversing the thin sample. In the low temperature phase, however, the peak displacement is substantial. The Bragg peak moves to its high temperature position within approximately 20 ps demonstrating that the unit cell is driven within this short time scale away from its monoclinic structure and towards the high temperature orthorhombic one.

The time dependence of the peak width and amplitude are shown in Fig. 4(c). The clear correlation between these two parameters results in an approximately constant integrated intensity throughout the transition [Fig. 4(d)]. Hence the structure factor is not significantly altered in the process and its variation can be neglected. The increase in peak width until about 15 ps indicates a decrease in correlation length, probably due to the coexistence of orthorhombic and monoclinic domains. The initial correlation length and amplitude recover within the subsequent 60 ps.

The fluence dependence for the (002) reflection at a fixed time delay of 100 ps is shown in Fig. 5. The peak is also fitted with a Lorentzian and the extracted peak position as a function of fluence is shown in the inset. Clear changes can be seen at $f \approx 2.4$ mJ/cm^2 and $f \approx 5$ mJ/cm^2, corresponding closely to the two critical fluences f_c and f_c' introduced in the previous section. For fluences below f_c the peak position remains fixed. Above f_c the peak gradually shifts and stabilizes approximately at the high temperature position for $f > f_c'$. Similar to the time dependence, the fluence dependence of the peak width and amplitude are anticorrelated, keeping the integrated intensity approximately constant [see inset Fig. 5(b)].

As stated in the previous section, the fluence f_c corresponds to the critical fluence necessary to melt the COO at the surface [19], indicating that the monoclinic-to-orthorhombic transition only occurs once the COO has entirely disappeared. This sharp threshold behavior is somewhat smeared between f_c and f_c' because of the excitation profile.

In Fig. 5(b), we compare the sample fraction in each phase with a simple model where we account for the excitation gradient [45]. To extract the volume fraction, two peaks are fitted to the data. The peak positions are constrained to the low and high fluence position, respectively, each peak being a measure of one of the phases, and the widths are assumed to be constant. The volume fraction of each phase is then given by the integrated intensity of its corresponding peak, normalized to the total intensity. The wide shoulder around $\phi = 0.5$ in the unpumped trace is taken as an additional background constant for all fluences.

We also calculate the critical depth z_c by inverting Eq. (1)

$$z_c = z_0 \ln(f_c/f_0), \quad (3)$$

and calculate for each fluence the volume fraction below and above f_c. This simple model describes the data well [lines in
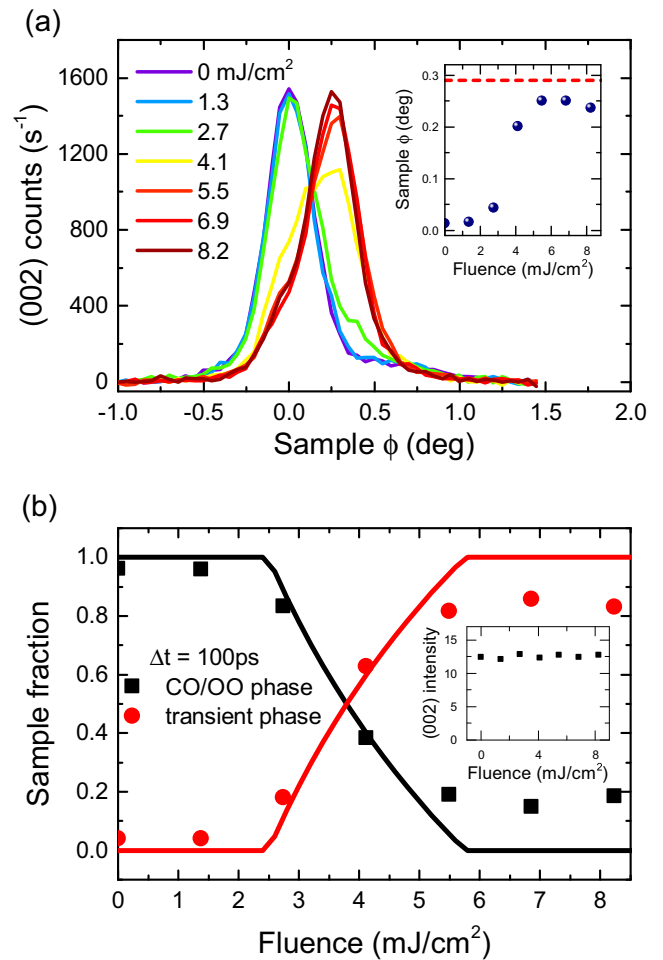

(a)

(b)

FIG. 5. (a) Fluence dependence of the (002) regular Bragg reflection 100 picoseconds after excitation. Data taken at 100 K. The inset shows the fitted peak position as a function of fluence. The red dashed line indicates the position of the high-temperature peak taken from Fig. 4 at $t = -1$ ps. (b) Fractions of each phase as a function of fluence 100 ps after excitation. They are extracted by fitting the data with a sum of two peaks whose centers are fixed at the peak position of the low and high temperature phases (symbols). The model (lines) takes into account the inhomogeneous excitation profile in the sample (see text for details). The inset shows the integrated intensity of the peak as a function of fluence.

Fig. 5(b)], demonstrating the threshold nature of the transition. The discrepancies at high fluence are attributed to the small changes of the structure factor and the partial recovery that starts already at about 50 ps after excitation [Fig. 4(b)].

This second step of the structural phase transition, the monoclinic-to-orthorhombic transition, takes place only for fluences exceeding a critical fluence f_c, when the COO and the superlattice are completely destroyed. As shown by the dynamics of the (002) reflection (Fig. 4), this step is much slower than the disappearance of the superstructure because it involves changes of the lattice constants which are carried by acoustic phonons and consequently limited by the speed of sound. As a matter of fact on these fast time scales only changes of the out-of-plane lattice constants occur whereas the in-plane lattice constants remain locked to the substrate [35].
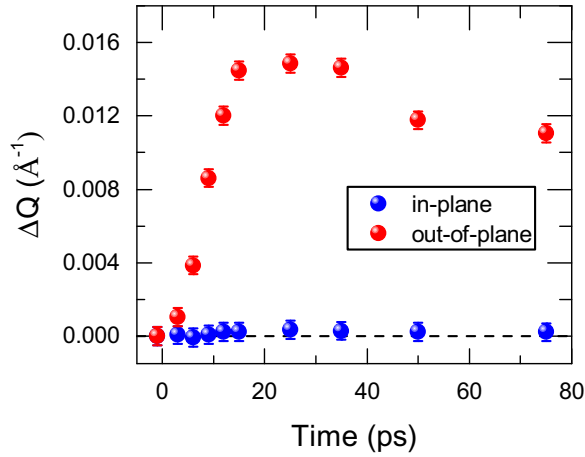
FIG. 6. Decomposition of the (002) peak position along the out-of-plane ($\bar{1}\bar{1}2$) and in-plane projections. These data are extracted from the reciprocal space analysis of the data in Fig. 4, taking advantage of the two-dimensional Pilatus pixel detector.

Indeed the decomposition of the Bragg peak position along the ($\bar{1}\bar{1}2$) out-of-plane and in-plane directions in Fig. 6 shows only a motion along the out-of-plane direction. The timescale on the order of 10 ps [Fig. 4(b)], is consistent with the time required for an acoustic strain wave to propagate at the speed of sound $v_s \approx 5$ nm/ps [44] across the 40 nm thickness of the film.

After the peak has reached the high temperature position, its intensity and width still evolve and relax back to their equilibrium value in the next 50 ps [see Fig. 4(c)]. The peak width is expected to follow a $t^{-1/2}$ dependence and displays indeed a behavior reasonably close to this trend [red line in Fig. 4(c)]. Such a time dependence stems from a $\sqrt{t}$ dependence of the domain size, which is predicted for domain growth dynamics following the quench of the order parameters [46–48]. The integrated intensity remains constant showing that the growth of the correlation length is not due to an increase of the transient phase fraction but is rather due to domain wall dynamics, which promotes larger domain size. The observation of both the $\sqrt{t}$ dependence of the domain size and a threshold as a function of fluence points toward a first-order-like description of this second step of the structural transition, while the initial COO melting and the subsequent collapse of the superlattice are continuous and were modeled with a single Landau-like order parameter [19].

These dynamics on a time scale of tens of picoseconds round up our understanding of the laser-induced phase transition: We have now identified three steps, each characterized by their relevant timescales. First, the charge and orbital order is destroyed by the photoexcitation of the electrons ($\tau_1 < 80$ fs) [19]. Second, the Jahn-Teller distortion collapses triggering the rearrangement of the unit cell in the high symmetry configuration ($\tau_2 \approx 0.5$ ps) [16,18,19]. Finally, within 10–20 ps this nonequilibrium state relaxes towards a thermodynamic metastable state, corresponding to the high temperature orthorhombic unit cell. In the adiabatic case these different components are indissociable, but they become separated in the time domain, as the change of each component is
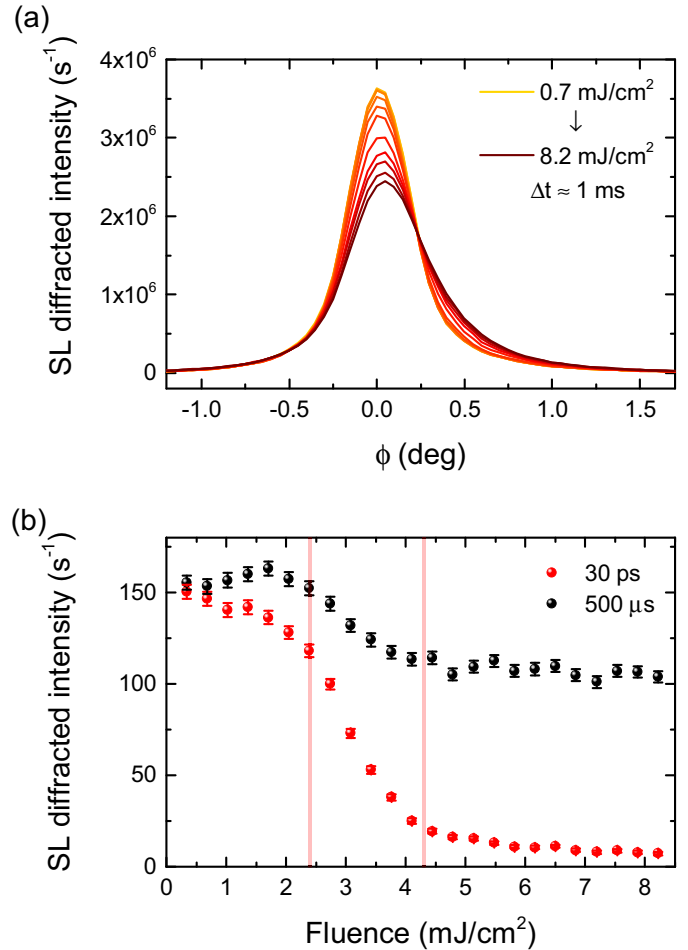

FIG. 7. (a) Rocking curves scans of the ($\bar{2}\frac{\bar{3}}{2}0$) superlattice peak measured for various pump fluences just before the arrival of the pump pulse. These data were taken at 1 kHz using 70 ps duration x-ray pulses (slicing mode off), explaining the much higher intensity. (b) Fluence dependence of the ($\bar{2}\frac{\bar{3}}{2}0$) reflection at $\phi = 0$ and 30 ps (red), respectively, 500 μs (black) after excitation. The 500 μs trace is usually taken as the unpumped reference for the pump-probe experiment at the FEMTO slicing source. The vertical lines indicate the two fluences f_c and f_c' respectively.

mediated by dynamics with different time scales. After this last step, the material is structurally in a configuration very close to that of the high temperature phase. The electronic and transport properties are, however, quite different. A metallic metastable state [1] and the rapid formation of ferromagnetic ordering [23] has been observed, differing significantly from the thermodynamic state above T_{COO}.

C. Recovery dynamics

In a pump-probe experiment the measured time dependent variable is usually normalized to the unperturbed value of the system before arrival of the pump, working under the assumption that the system fully recovers between subsequent pump pulses. Hence most studies concentrate on the pump induced relative changes (see Fig. 2 for example). In Fig. 7(a), we plot rocking curves of the ($\bar{2}\frac{\bar{3}}{2}0$) SL reflection for a set of fluences taken just before the arrival time of the next pump,
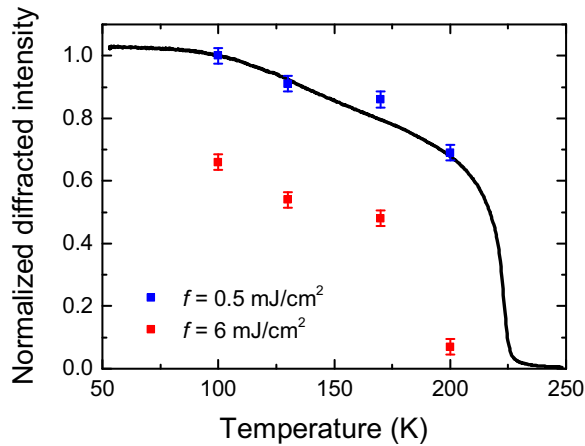
FIG. 8. Static temperature dependence of the superlattice peak compared to the peak intensity at 500 μs for two different fluences. The data are normalized to the unpumped intensity at 100 K.

corresponding to a delay of almost 1 ms after the previous pump pulse. It is clear that the system at higher pump fluences does not fully return to the ground state. This reduction is not due to permanent damage because the intensity fully recovers when blocking the pump. The broader width at the highest fluences indicates smaller domain sizes and the slight shift possibly a marginal increase of the base temperature. The integrated intensity overall decreases by about 15% at the highest fluences. Considering that the integrated intensity of the (002) reflection remains constant as a function of fluence [inset of Fig. 5(b)], we conclude that these changes originate exclusively from smaller ordered domains, which results in an increased number of domain walls that do not contribute to the superlattice reflection.

Figure 7(b) shows the maximum intensity of the $(\bar{2}\frac{\bar{3}}{2}0)$ reflection as a function of fluence 30 ps and 500 μs after excitation. The intensity at $t = 30$ ps shows the expected kink at f_c and vanishes around f_c' when the COO is melted throughout the film. The unpumped reference (500 μs curve, black circles) remains stable until the critical fluence is reached and then continuously drops until f_c'. For larger fluence it again remains constant at about 65% of its equilibrium value. This decrease in intensity is only partially compensated by the increased width [Fig. 7(a)].

Upon the observation of such long-lived dynamics, the pump-probe repetition rate ideally would have to be reduced [22]. This was unfortunately not feasible here due to the very low flux of the slicing source. Although we should be cautious in the treatment of data at fluences above f_c, there is no indication that the phase after 1 ms is substantially different from the original COO phase. Fluence scans of the maximum superlattice intensity, as shown in Fig. 7(b), were taken for a few temperatures between 100 and 200 K. In Fig. 8, we report the diffracted intensities measured 500 μs after excitation as a function of temperature and compare them to the static temperature dependence of the superlattice peak. For fluence smaller than f_c, the temperature dependence of the sample follows that of the equilibrium case. At 6 mJ/cm^2, the diffracted intensity is reduced and at 200 K the superlattice does not restore anymore, suggesting that the base temperature

has increased by $\approx$20 K. Since the specific heat depends approximately linearly on temperature in the range between 100 to 200 K [49] and assuming that the cooling efficiency does not change over this temperature range, we estimate a temperature increase of $\approx$40 K at 100 K for the same pump fluence. From the static temperature dependence, we expect a decrease of the peak intensity of about 10%, which compares well to the 12% decrease of the integrated intensity extracted from the rocking curve at 6 mJ/cm^2 in Fig. 7(a). The further decrease of the peak amplitude comes from the reduction of the correlation length. We thus appear to observe only an increase of the average temperature and a reduction of the domain size. With this in mind, we argue that the sample turns to the COO phase and that we can discuss some aspects of the critical behavior and the recovery dynamics.

The completion of the transition above f_c significantly modifies the relaxation dynamics. For example, the time required to recover the COO superlattice increases by many orders of magnitude [Fig. 7(b)]. These observations echo a similar study of the antiferromagnetic dynamics in PCMO, where the recovery timescales span from tens of nanoseconds at low fluence to seconds at high excitation [22]. Our interpretation is that in the partially melted volume fraction the remaining order favors the relaxation to the ground state, reinforced by the still monoclinic domains. Even though the order is reduced, the symmetry is still broken for $f < f_c$, which seeds the recovery. At high excitation levels new nucleation centers have to be created before the low temperature phase can recover. Hence in analogy to supercooling, the relaxation is significantly delayed. This view is in accordance with the first-order nature of the COO transition. In equilibrium the antiferromagnetic transition is, however, second order and should not display the same hysteretic behavior. In addition the previously-observed glasslike recovery of the magnetic phase [22] is characteristic of a first order transition, contradicting again the static picture. These observations show that the antiferromagnetic state cannot grow without the pre-establishment of the charge and orbital order. The magnetic transition is thus limited by the time the COO state needs to emerge, hence displaying the same first-order behavior and the same delay in its recovery.

D. Connection to ferromagnetism

It has been proposed that the ferromagnetic correlations possibly emerge within the first 120 fs after excitation [23,24] and the antiferromagnetic magnetic order was shown to be suppressed on a timescale faster than 250 fs [21]. These timescales are limited by the experimental resolutions and are compatible with the fast reduction of the COO that we observe. Interestingly, a fast rise of the magnetization is only found above a threshold fluence $f_{th} = 2.5$ mJ/cm^2, which matches surprisingly well the critical fluence f_c found here for the COO melting and the structural phase transition. Below this threshold, the ferromagnetic volume increases on a slower picosecond timescale, assigned to thermal effects. Outside the COO region of the phase diagram, manganites often develop a ferromagnetic or canted ordering at low temperature, which, in association with the double exchange mechanism, leads to the observed metallic behavior [14]. Due to the small ionic size of Pr and Ca, the thermodynamic ferromagnetic phase

in PCMO is, somewhat unusually, insulating. In cuprates the charge ordered state was shown to hamper the superconducting dome [50,51]. Similarly here, the ferromagnetic metallic state may thus be hindered by the COO and may become a hidden metastable state that is only accessible by applying a magnetic field for example or by nonthermal melting of the COO via ultrafast photoexcitation.

IV. SUMMARY AND CONCLUSION

We performed a detailed study of the structural dynamics after melting of the COO in PCMO. While the superlattice intensity related to the charge and orbital order decreases continuously with fluence, the monoclinic-to-orthorhombic transition is slower and displays a first-order-like threshold behavior. Both components of the photoinduced transition are, however, linked to the same critical excitation fluence. Comparing these results to previous studies of the COO and magnetic dynamics, we find that all of the photoinduced dynamics are actually related to the same critical fluence f_c, depicting a comprehensive picture of the photoinduced transition in manganites, where the charge, structure, and spin dynamics fit together.

Finally the completion of the phase transition for fluences above f_c is also found to provoke a significant delay in the recovery dynamics that is well explained by the first-order nature of the thermodynamic structural transition. We also argue that the charge and orbitally ordered phase is a necessary precursor for the establishment of the antiferromagnetic order in manganites, as the emergence of the antiferromagnetic order is limited by the recovery of the charge and orbital order.

[1] M. Fiebig, K. Miyano, Y. Tomioka, and Y. Tokura, Visualization of the local insulator-metal transition in $Pr_{0.7}Ca_{0.3}MnO_3$, Science **280**, 1925 (1998).

[2] A. Cavalleri, C. Tóth, C. W. Siders, J. A. Squier, F. Ráksi, P. Forget, and J. C. Kieffer, Femtosecond Structural Dynamics in VO_2 During an Ultrafast Solid-Solid Phase Transition, Phys. Rev. Lett. **87**, 237401 (2001).

[3] A. Tomeljak, H. Schäfer, D. Städter, M. Beyer, K. Biljakovic, and J. Demsar, Dynamics of Photoinduced Charge-Density-Wave to Metal Phase Transition in $K_{0.3}MoO_3$, Phys. Rev. Lett. **102**, 066404 (2009).

[4] V. R. Morrison, R. P. Chatelain, K. L. Tiwari, A. Hendaoui, A. Bruhács, M. Chaker, and B. J. Siwick, A photoinduced metal-like phase of monoclinic VO_2 revealed by ultrafast electron diffraction, Science **346**, 445 (2014).

[5] D. Fausti, R. I. Tobey, N. Dean, S. Kaiser, A Dienst, M. C. Hoffmann, S. Pyon, T. Takayama, H. Takagi, and A. Cavalleri, Light-induced superconductivity in a stripe-ordered cuprate, Science **331**, 189 (2011).

[6] R. Mankowsky, A. Subedi, M. Först, S. O. Mariager, M. Chollet, H. T. Lemke, J. S. Robinson, J. M. Glownia, M. P. Minitti, A. Frano *et al.*, Nonlinear lattice dynamics as a basis for enhanced superconductivity in $YBa_2Cu_3O_{6.5}$, Nature (London) **516**, 71 (2014).

[7] M. Mitrano, A. Cantaluppi, D. Nicoletti, S. Kaiser, A. Perucchi, S. Lupi, P. Di Pietro, D. Pontiroli, M. Riccò, S. R. Clark *et al.*, Possible light-induced superconductivity in K_3C_60 at high temperature. Nature (London) **530**, 461 (2016).

[8] D. S. Rana, I. Kawayama, K. Mavani, K. Takahashi, H. Murakami, and M. Tonouchi, Understanding the nature of ultrafast polarization dynamics of ferroelectric memory in the multiferroic $BiFeO_3$, Adv. Mater. **21**, 2881 (2009).

[9] R. Mankowsky, A. von Hoegen, M. Först, and A. Cavalleri, Ultrafast Reversal of the Ferroelectric Polarization, Phys. Rev. Lett. **118**, 197601 (2017).

[10] M. Finazzi, M. Savoini, A. R. Khorsand, A. Tsukamoto, A. Itoh, L. Duò, A. Kirilyuk, Th. Rasing, and M. Ezawa, Laser-Induced Magnetic Nanostructures with Tunable Topological Properties, Phys. Rev. Lett. **110**, 177205 (2013).

[11] T. Kubacka, J. A. Johnson, M. C. Hoffmann, C. Vicario, S. de Jong, P. Beaud, S. Grübel, S.-W. Huang, L. Huber, L. Patthey, Y.-D. Chuang, J. J. Turner, G. L. Dakovski, W.-S. Lee, M. P. Minitti, W. Schlotter, R. G. Moore, C. P. Hauri, S. M. Koohpayeh, V. Scagnoli, G. Ingold, S. L. Johnson, and U. Staub, Large-amplitude spin dynamics driven by a THz pulse in resonance with an electromagnon, Science **343**, 1333 (2014).

[12] G. Auböck and M. Chergui, Sub-50-fs photoinduced spin crossover in $[Fe (bpy)_3]^{2+}$, Nature Chemistry **7**, 629 (2015).

[13] S. Baierl, J. H. Mentink, M. Hohenleutner, L. Braun, T.-M. Do, C. Lange, A. Sell, M. Fiebig, G. Woltersdorf, T. Kampfrath, and R. Huber, Terahertz-Driven Nonlinear Spin Response of Antiferromagnetic Nickel Oxide, Phys. Rev. Lett. **117**, 197201 (2016).

[14] E. Dagotto, *Nanoscale Phase Separation and Colossal Magnetoresistance: The Physics of Manganites and Related Compounds* (Springer, Berlin, 2003).

[15] D. Polli, M. Rini, S. Wall, R. W. Schoenlein, Y. Tomioka, Y. Tokura, G. Cerullo, and A. Cavalleri, Coherent orbital waves in the photoinduced insulator–metal dynamics of a magnetoresistive manganite, Nat. Mater. **6**, 643 (2007).

[16] P. Beaud, S. L. Johnson, E. Vorobeva, U. Staub, R. A. De Souza, C. J. Milne, Q. X. Jia, and G. Ingold, Ultrafast Structural Phase Transition Driven by Photoinduced Melting of Charge and Orbital Order, Phys. Rev. Lett. **103**, 155702 (2009).

[17] K. Miyano, T. Tanaka, Y. Tomioka, and Y. Tokura, Photoinduced Insulator-To-Metal Transition in a Perovskite Manganite, Phys. Rev. Lett. **78**, 4257 (1997).

[18] A. Caviezel, U. Staub, S. L. Johnson, S. O. Mariager, E. Möhr-Vorobeva, G. Ingold, C. J. Milne, M. Garganourakis, V. Scagnoli, S. W. Huang, Q. X. Jia, S.-W. Cheong, and P. Beaud, Femtosecond dynamics of the structural transition in mixed valence manganites, Phys. Rev. B **86**, 174105 (2012).

[19] P. Beaud, A. Caviezel, S. O. Mariager, L. Rettig, G. Ingold, C. Dornes, S. W. Huang, J. A. Johnson, M. Radovic, T. Huber *et al.*, A time-dependent order parameter for ultrafast photoinduced phase transitions, Nat. Mater. **13**, 923 (2014).

[20] H. Ehrke, R. I. Tobey, S. Wall, S. A. Cavill, M. Först, V. Khanna, Th. Garl, N. Stojanovic, D. Prabhakaran, A. T. Boothroyd, M. Gensch, A. Mirone, P. Reutler, A. Revcolevschi, S. S. Dhesi, and A. Cavalleri, Photoinduced Melting of Antiferromagnetic Order in La$_{0.5}$Sr$_{1.5}$MnO$_4$ Measured using Ultrafast Resonant Soft X-Ray Diffraction, Phys. Rev. Lett. **106**, 217401 (2011).

[21] M. Först, R. I. Tobey, S. Wall, H. Bromberger, V. Khanna, A. L. Cavalieri, Y.-D. Chuang, W. S. Lee, R. Moore, W. F. Schlotter, J. J. Turner, O. Krupin, M. Trigo, H. Zheng, J. F. Mitchell, S. S. Dhesi, J. P. Hill, and A. Cavalleri, Driving magnetic order in a manganite by ultrafast lattice excitation, Phys. Rev. B **84**, 241104 (2011).

[22] S. Y. Zhou, M. C. Langner, Y. Zhu, Y.-D. Chuang, M. Rini, T. E. Glover, M. P. Hertlein, A. G. C. Gonzalez, N. Tahir, Y. Tomioka *et al.*, Glass-like recovery of antiferromagnetic spin ordering in a photoexcited manganite Pr$_{0.7}$Ca$_{0.3}$MnO$_3$, Sci. Rep. **4**, 4050 (2014).

[23] T. Li, A. Patz, L. Mouchliadis, J. Yan, T. A. Lograsso, I. E. Perakis, and J. Wang, Femtosecond switching of magnetism via strongly correlated spin-charge quantum excitations, Nature (London) **496**, 69 (2013).

[24] P. C. Lingos, A. Patz, T. Li, G. D. Barmparis, A. Keliri, M. D. Kapetanakis, L. Li, J. Yan, J. Wang, and I. E. Perakis, Correlating quasiparticle excitations with quantum femtosecond magnetism in photoexcited nonequilibrium states of insulating antiferromagnetic manganites, Phys. Rev. B **95**, 224432 (2017).

[25] M. Rini, Y. Zhu, S. Wall, R. I. Tobey, H. Ehrke, T. Garl, J. W. Freeland, Y. Tomioka, Y. Tokura, A. Cavalleri, and R. W. Schoenlein, Transient electronic structure of the photoinduced phase of Pr$_{0.7}$Ca$_{0.3}$MnO$_3$ probed with soft x-ray pulses, Phys. Rev. B **80**, 155113 (2009).

[26] V. Esposito, M. Fechner, R. Mankowsky, H. Lemke, M. Chollet, J. M. Glownia, M. Nakamura, M. Kawasaki, Y. Tokura, U. Staub, P. Beaud, and M. Först, Nonlinear Electron-Phonon Coupling in Doped Manganites, Phys. Rev. Lett. **118**, 247601 (2017).

[27] M. Tokunaga, N. Miura, Y. Tomioka, and Y. Tokura, High-magnetic-field study of the phase transitions of R_{1-x}Ca$_x$MnO$_3$ (R = Pr, Nd), Phys. Rev. B **57**, 5259 (1998).

[28] V. Kiryukhin, D. Casa, J. P. Hill, B. Keimer, A. Vigliante, Y. Tomioka, and Y. Tokura, An x-ray-induced insulator–metal transition in a magnetoresistive manganite, Nature (London) **386**, 813 (1997).

[29] M. Garganourakis, V. Scagnoli, S. W. Huang, U. Staub, H. Wadati, M. Nakamura, V. A. Guzenko, M. Kawasaki, and Y. Tokura, Imprinting Magnetic Information in Manganites with X Rays, Phys. Rev. Lett. **109**, 157203 (2012).

[30] T. Elovaara, S. Majumdar, H. Huhtinen, and P. Paturi, Photoinduced colossal magnetoresistance under substantially reduced magnetic field, Adv. Funct. Mater. **25**, 5030 (2015).

[31] R. J. Goff and J. P. Attfield, Charge ordering in half-doped manganites, Phys. Rev. B **70**, 140404 (2004).

[32] M. v. Zimmermann, J. P. Hill, D. Gibbs, M. Blume, D. Casa, B. Keimer, Y. Murakami, Y. Tomioka, and Y. Tokura, Interplay Between Charge, Orbital, and Magnetic Order in Pr$_{1-x}$Ca$_x$MnO$_3$, Phys. Rev. Lett. **83**, 4872 (1999).

[33] All the Miller indices in this paper are given with respect to the high temperature orthorhombic cell.

[34] U. Staub, M. García-Fernández, Y. Bodenthin, V. Scagnoli, R. A. De Souza, M. Garganourakis, E. Pomjakushina, and K. Conder, Orbital and magnetic ordering in Pr$_{1-x}$Ca$_x$MnO$_3$ and Nd$_{1-x}$Sr$_x$MnO$_3$ manganites near half doping studied by resonant soft x-ray powder diffraction, Phys. Rev. B **79**, 224419 (2009).

[35] D. Okuyama, M. Nakamura, Y. Wakabayashi, H. Itoh, R. Kumai, H. Yamada, Y. Taguchi, T. Arima, M. Kawasaki, and Y. Tokura, Epitaxial-strain effect on charge/orbital order in Pr$_{0.5}$Ca$_{0.5}$MnO$_3$ films, Appl. Phys. Lett. **95**, 152502 (2009).

[36] P. Beaud, S. L. Johnson, A. Streun, R. Abela, D. Abramsohn, D. Grolimund, F. Krasniqi, T. Schmidt, V. Schlott, and G. Ingold, Spatiotemporal Stability of a Femtosecond Hard–X-Ray Undulator Source Studied by Control of Coherent Optical Phonons, Phys. Rev. Lett. **99**, 174801 (2007).

[37] S. L. Johnson, P. Beaud, C. J. Milne, F. S. Krasniqi, E. S. Zijlstra, M. E. Garcia, M. Kaiser, D. Grolimund, R. Abela, and G. Ingold, Nanoscale Depth-Resolved Coherent Femtosecond Motion in Laser-Excited Bismuth, Phys. Rev. Lett. **100**, 155501 (2008).

[38] M. Saes, F. Van Mourik, W. Gawelda, M. Kaiser, M. Chergui, C. Bressler, D. Grolimund, R. Abela, T. E. Glover, P. A Heimann *et al.*, A setup for ultrafast time-resolved x-ray absorption spectroscopy, Rev. Sci. Instrum. **75**, 24 (2004).

[39] B. Henrich, A. Bergamaschi, C. Broennimann, R. Dinapoli, E. F. Eikenberry, I. Johnson, M. Kobas, P. Kraft, A. Mozzanica, and B. Schmitt, Pilatus: A single photon counting pixel detector for x-ray applications, Nucl. Instr. Methods Phys. Res. Sec. A **607**, 247 (2009).

[40] A. Caviezel, S. O. Mariager, S. L. Johnson, E. Möhr-Vorobeva, S. W. Huang, G. Ingold, U. Staub, C. J. Milne, S.-W. Cheong, and P. Beaud, Identification of coherent lattice modulations coupled to charge and orbital order in a manganite, Phys. Rev. B **87**, 205104 (2013).

[41] H. Matsuzaki, H. Uemura, M. Matsubara, T. Kimura, Y. Tokura, and H. Okamoto, Detecting charge and lattice dynamics in photoinduced charge-order melting in perovskite-type manganites using a 30-femtosecond time resolution, Phys. Rev. B **79**, 235131 (2009).

[42] D. Lim, V. K. Thorsmølle, R. D. Averitt, Q. X. Jia, K. H. Ahn, M. J. Graf, S. A. Trugman, and A. J. Taylor, Coherent optical and acoustic phonon generation correlated with the charge-ordering phase transition in La$_{1-x}$Ca$_x$MnO$_3$, Phys. Rev. B **71**, 134403 (2005).

[43] V. A. Amelitchev, B. Güttler, O. Yu. Gorbenko, A. R. Kaul, A. A. Bosak, and A. Yu. Ganin, Structural and chemical analysis of colossal magnetoresistance manganites by raman spectrometry, Phys. Rev. B **63**, 104430 (2001).

[44] Y. P. Gaidukov, N. P. Danilova, A. A. Mukhin, and A. M. Balbashov, Behavior of sound velocities in the compounds

La$_{1-x}$Sr$_x$MnO$_3$ near magnetic and structural phase transitions, JETP Lett. **68**, 153 (1998).

[45] E. Möhr-Vorobeva, S. L. Johnson, P. Beaud, U. Staub, R. De Souza, C. Milne, G. Ingold, J. Demsar, H. Schaefer, and A. Titov, Nonthermal Melting of a Charge Density Wave in TiSe$_2$, Phys. Rev. Lett. **107**, 036403 (2011).

[46] G. S. Grest, M. P. Anderson, and D. J. Srolovitz, Domain-growth kinetics for the Q-state potts model in two and three dimensions, Phys. Rev. B **38**, 4752 (1988).

[47] L.-Q. Chen and W. Yang, Computer simulation of the domain dynamics of a quenched system with a large number of nonconserved order parameters: The grain-growth kinetics, Phys. Rev. B **50**, 15752 (1994).

[48] C. Laulhé, T. Huber, G. Lantz, A. Ferrer, S. O. Mariager, S. Grübel, J. Rittmann, J. A. Johnson, V. Esposito, A. Lübcke *et al.*, Ultrafast Formation of a Charge Density Wave State in 1

T-TaS$_2$: Observation at Nanometer Scales Using Time-Resolved X-Ray Diffraction, Phys. Rev. Lett. **118**, 247401 (2017).

[49] V. Hardy, A. Maignan, S. Hebert, and C. Martin, Calorimetric and magnetic investigations of the metamagnet Pr$_{0.5}$Ca$_{0.5}$Mn$_{0.95}$Ga$_{0.05}$O$_3$, Phys. Rev. B **67**, 024401 (2003).

[50] J. Chang, E. Blackburn, A. T. Holmes, N. B. Christensen, J. Larsen, J. Mesot, R. Liang, D. A. Bonn, W. N. Hardy, A. Watenphul *et al.*, Direct observation of competition between superconductivity and charge density wave order in YBa$_2$Cu$_3$O$_{6.67}$, Nat. Phys. **8**, 871 (2012).

[51] E. H. da Silva Neto, P. Aynajian, A. Frano, R. Comin, E. Schierle, E. Weschke, A. Gyenis, J. Wen, J. Schneeloch, Z. Xu *et al.*, Ubiquitous interplay between charge ordering and high-temperature superconductivity in cuprates, Science **19**, 1243479 (2013).